

Optical and Electrical Characterization of Er/Yb-Doped Porous Silicon for Advanced Photovoltaic Applications

Aldo M. C. Gomes and Danilo R. Huanca*

This study examines the optical and electrical properties of erbium- and ytterbium-doped porous silicon (PS). Reflectance, absorbance, and impedance measurements reveal that doping with 0.005 M $\text{Er}(\text{NO}_3)_3$ and $\text{Yb}(\text{NO}_3)_3$ significantly enhances absorbance, with Yb achieving a 225% increase compared to undoped PS. Thermal oxidation further boosts absorbance by up to 300% in the near-infrared (NIR) region, attributed to the formation of $\text{Er}_2\text{Si}_2\text{O}_7$, Er_2SiO_5 , and $\text{Yb}_2\text{Si}_2\text{O}_7$, confirmed by energy dispersive X-ray spectroscopy and X-ray diffraction. Despite these changes, Kubelka–Munk analysis shows no significant bandgap alteration for indirect transitions. The improved optical absorption, particularly in the NIR, suggests potential for enhancing photovoltaic device efficiency. Electrically, impedance spectroscopy indicates that Er/Yb doping improves charge transfer in liquid media, though the ternary compounds reduce layer conductivity. These findings demonstrate that rare earth doping enhances both optical and electrical properties of PS, making it promising for optoelectronic applications, especially in NIR-sensitive photovoltaics.

1. Introduction

Porous silicon (PS) has garnered considerable attention due to its highly tunable physical properties, which are governed by structural parameters such as porosity, layer thickness, and the dimensions of residual silicon crystallites within the porous network.^[1] These characteristics directly influence its photoluminescent behavior, making PS an attractive platform for applications in optoelectronics and sensing technologies.^[1–3] In recent years, the incorporation of rare-earth (RE) elements into PS matrices has emerged as an effective strategy to tailor and enhance its luminescent properties.^[4–7] Among these, erbium

(Er) has been widely studied, particularly for its applications in telecommunications, with various fabrication and characterization techniques—especially electrochemical methods—employed to investigate its performance.^[4–9] Despite the focus on luminescence, the electrical properties of RE-doped PS remain underexplored, though they are critical for advancing applications in light-emitting devices and photovoltaics, where efficient light absorption and charge transport are essential.

Notably, studies by Atyaoui et al.^[10–12] demonstrated that doping PS with elements such as lanthanum (La) and cerium (Ce) can enhance both optical and electrical performance. RE-doped PS systems have shown promise as alternatives to conventional antireflection coatings due to their unique optical behaviors, including down- and up-conversion mechanisms.^[9,13]

Furthermore, these materials often exhibit increased surface roughness,^[12,14] a feature that can further improve light trapping and photoconversion efficiency in solar cells.

To date, most research has prioritized RE dopants exhibiting visible-range photoluminescence, particularly focusing on their impact on absorption and surface morphology.^[10–12,14] However, Er and ytterbium (Yb) stand out for their strong infrared emission, indicating potential for enhanced spectral absorption in the near-infrared region. Despite this, studies investigating the electrical characteristics of Er- and Yb-doped PS are limited, with only a few exceptions (e.g., Mula et al.).^[7] Prior work has primarily addressed photoluminescence, often overlooking electrical performance—despite its relevance for photovoltaic applications.

This study aims to fill this gap by systematically analyzing the optical and electrical properties of RE-doped PS fabricated via cyclic voltammetry, with a focus on the effects of Er and Yb incorporation on reflectance, absorbance, and impedance behavior. While our current investigation centers on absorbance and electrical measurements, we hypothesize that Er and Yb dopants may elicit similar enhancements to those previously observed with Ce, La, and Sm. Our results indicate notable improvements in both optical and electrical performance, underscoring the potential of RE-doped PS for next-generation optoelectronic applications, including light-emitting devices and high-efficiency solar cells.

A. M. C. Gomes, D. R. Huanca
 Laboratory of Devices and Micro and Nanostructured Systems (LADISμNE), Institute of Physics and Chemistry
 Federal University of Itajubá
 Av. BPS 1303, Itajubá 37500-903, Minas Gerais, Brazil
 E-mail: droqueh@unifei.edu.br

 The ORCID identification number(s) for the author(s) of this article can be found under <https://doi.org/10.1002/pssa.202500414>.

© 2025 The Author(s). physica status solidi (a) applications and materials science published by Wiley-VCH GmbH. This is an open access article under the terms of the Creative Commons Attribution License, which permits use, distribution and reproduction in any medium, provided the original work is properly cited.

DOI: [10.1002/pssa.202500414](https://doi.org/10.1002/pssa.202500414)

2. Results and Discussions

2.1. Sample Fabrication

After pore formation, the thickness and porosity of the samples were estimated by fitting the reflectance spectrum using the single absorbing layer model onto a substrate,^[15] where the effective refractive index was computed using the Looyenga effective medium approach.^[16] From this procedure, the thickness and porosity were estimated to be equal to $(21.6 \pm 2.3) \mu\text{m}$ and $(54.9\% \pm 4.2\%)$, respectively. The roughness of the air/PS and PS/Si interfaces was found to be (0.043 ± 0.012) and $(0.036 \pm 0.010) \mu\text{m}$.

Prior to the RE deposition, a cyclic voltammetry analysis was performed at a potential sweep ranging from 10 to 500 mV s⁻¹ (Figure 1). It was observed that Er deposition occurs in a potential interval of -0.4 and 0.1 V (Figure 1a), depending on the sweep potential, which also influences the total current even at the maximum.^[17,18] In contrast, Yb exhibits a broader electrochemical potential window ranging from approximately -0.45 to 0.45 V (Figure 1b), and a higher maximum current intensity of $\approx 2.5 \times 10^{-5} \text{ A}$ at 500 mV s^{-1} compared to Er ($\approx 1.3 \times 10^{-5} \text{ A}$). This difference can be attributed to the more favorable reduction potential of Yb and faster electron transfer kinetics.^[19]

The lack of symmetry of these curves evidences a nonreversible reaction system. In semiconductor electrochemistry, this behavior is linked to the depletion layer effect, since it becomes greater at backward polarization due to the increase in both depletion layer width and built-in potential barrier^[20] disabling the charge transfer from electrolyte. According to the literature,^[17,18] even in this case of irreversible systems, the maximum current density is proportional to the square root of the sweep potential (Equation 1). This trend was observed in our case (inset in Figure 1a).

$$j_p = -nFAC^0 D_0^{1/2} v^{1/2} \left(\frac{an' F}{RT} \right)^{1/2} \quad (1)$$

where F is the Faraday constant and R and T are the universal gas constant and temperature, respectively. D_0 and n are the

diffusion coefficient and the number of electrons participating in the charge transfer reaction. C^0 is the concentration of the reactant, and n' is the number of electrons transferred in the rate-determining step. A is the electrode area.

Regarding the cyclic voltammetry curve, these results are comparable to those reported by Petrovich et al.^[8] Since the redox potential for erbium phases is below -2.0 V,^[21] the marked shift of deposition potential to less negative potential was attributed to the contribution of NO_3^- ions and $\text{C}_2\text{H}_5\text{O}^-$ species from the strong acid salt $\text{Er}(\text{NO}_3)_3$ and ethanol.

2.2. Morphological and Chemical Characterization

Figure 2a,b shows the top-view SEM images captured from the surface of the sample PS:Er(0.005) and PS:Yb(0.005), respectively, immersed in 0.005 M $\text{RE}(\text{NO}_3)_3$ for RE (= Er, Yb) deposition. The EDS analysis (Figure 2c) reveals the spatial homogeneous distribution of Er along the entire surface, being the predominant silicon and oxygen, as well as the presence of copper (Figure 2c). The chemical quantification of this sample indicates 51.8% of silicon, 45.5% of oxygen, 2.2% of Cu, and also 0.6% Er. Since in our procedure Cu was not employed, the source of it seems to be a local contaminant. Higher concentrations of Er were recorded from the sample treated using 0.02 M $\text{Er}(\text{NO}_3)_3$, labeled as PS:Er(0.02).

Figure 2d exhibits the top view of PS:Yb(0.005) and shows the significant differences in surface morphology because the presence of Yb is noticeable. The EDS mapping and spectrum of this sample (Figure 2d) reveal the presence of about 3.44% of Yb and around 10% of F in the regions closer to the white spots, suggesting that the presence of fluorine acts as catalyst for the formation of this Yb-rich region. Also, 60.33% of Si and 14.51% of oxygen are also observed. The presence of F is attributed to its retention within the pores, as the RE deposition was performed immediately after pore formation. Notably, no chemical reaction between F and Er is observed, which explains the absence of Er-rich regions in the analytical results.

Regarding the Cu peak, no evidence of this element was detected in the RBS analysis (Figure 3). This observation,

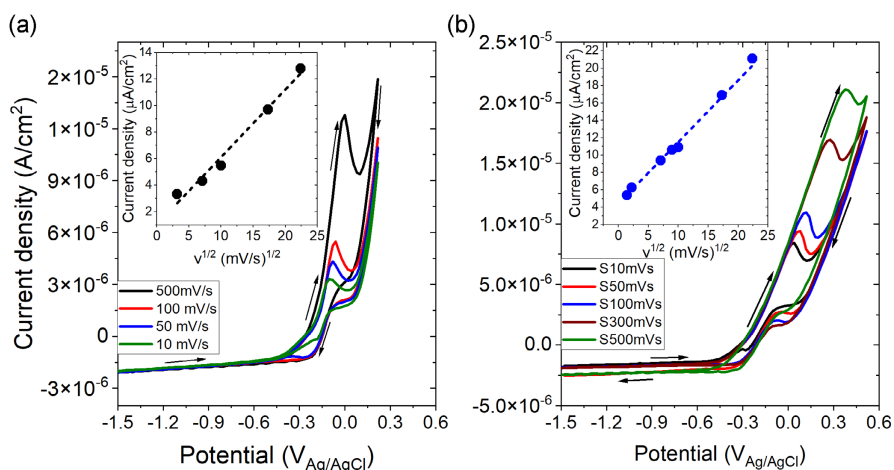


Figure 1. Cyclic voltammetry recorded using PS as the working electrode and an electrolyte solution of a) 0.02 M $\text{Er}(\text{NO}_3)_3$ and b) 0.005 M $\text{Yb}(\text{NO}_3)_3$ both dissolved in ethanol.

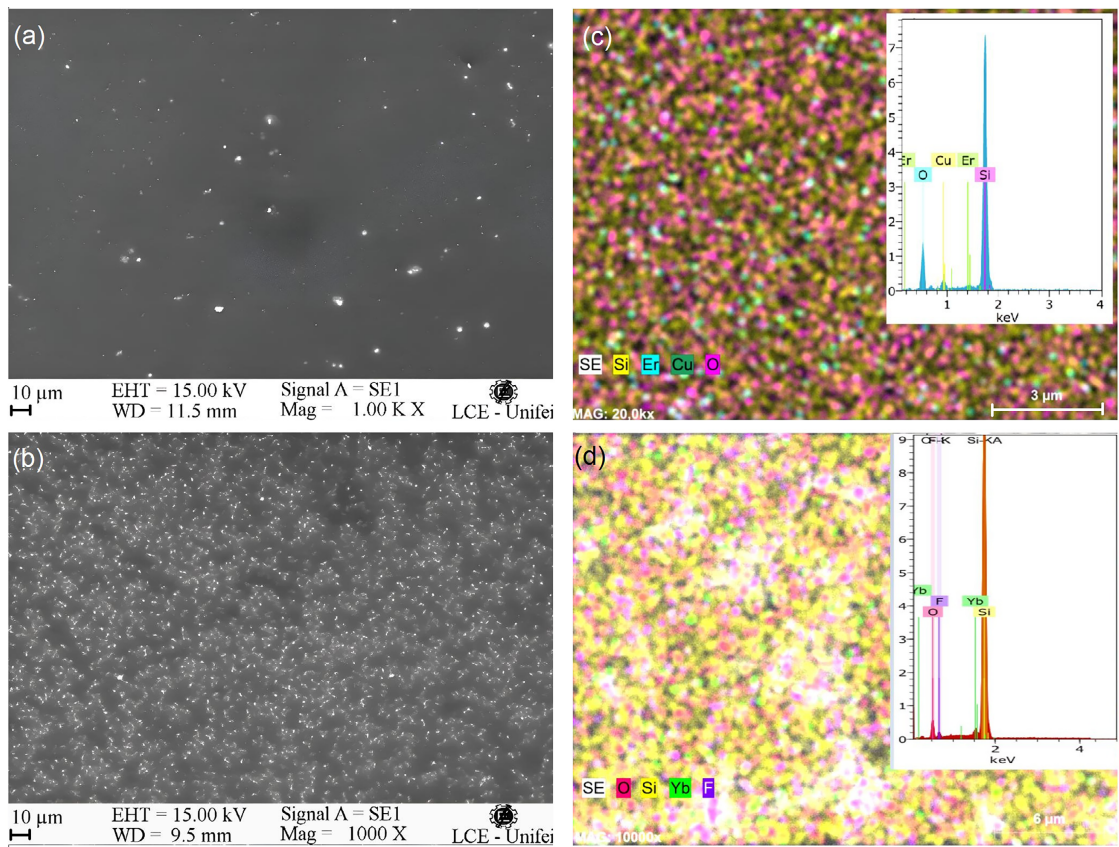


Figure 2. Top-view SEM images recorded from the sample doping using a) 0.005 M $\text{Er}(\text{NO}_3)_3$ and b) 0.005 M $\text{Yb}(\text{NO}_3)_3$ along with c,d) their respective EDS mapping and peaks.

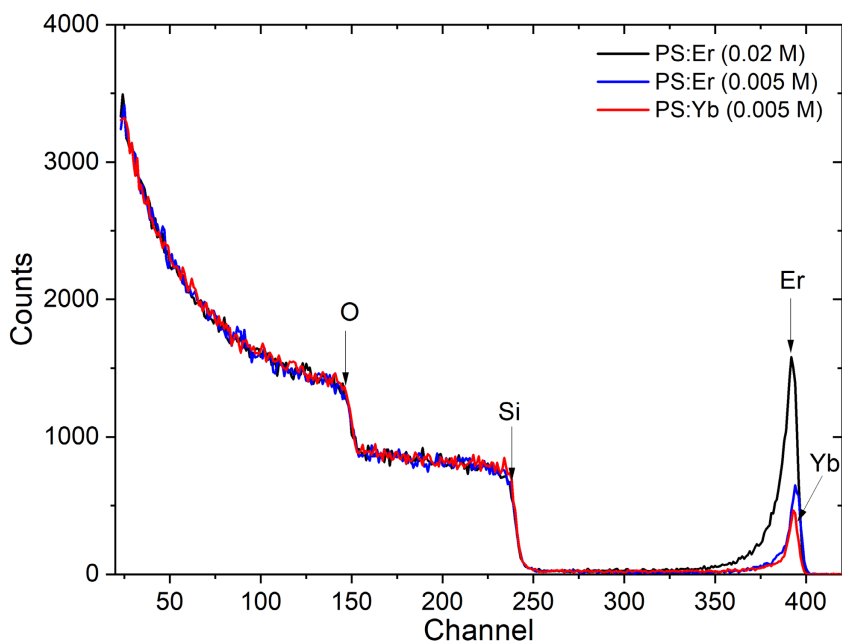


Figure 3. RBS spectra of erbium and ytterbium containing porous silicon.

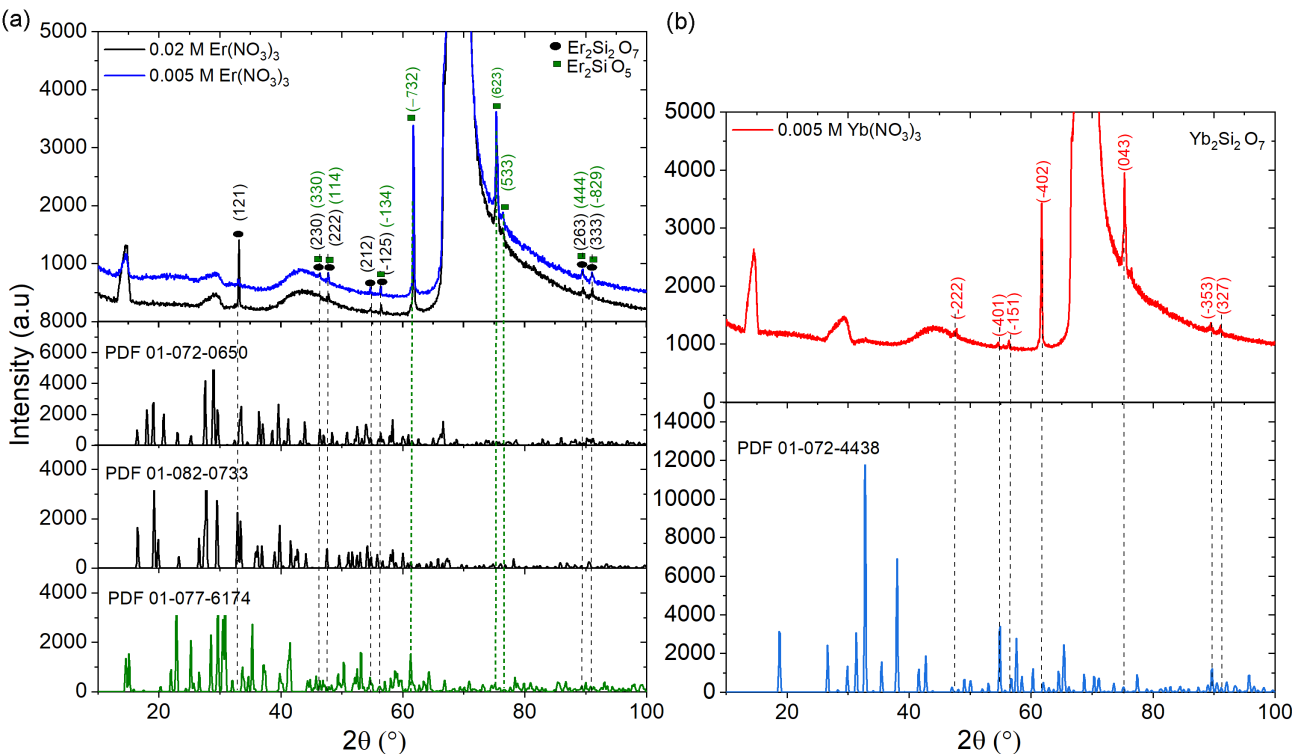


Figure 4. XRD pattern recorded from a) erbium and b) ytterbium containing porous silicon.

combined with the absence of Cu-related peaks or associated phases in the X-ray diffraction (XRD) pattern (Figure 4), supports the hypothesis of localized Cu contamination. Instead, the XRD pattern exhibits distinct peaks corresponding to the ternary compound $\text{Er}_2\text{Si}_2\text{O}_7$ (black circles in Figure 4a), consistent with the findings of Smolin and Shepelev (PDF 01-072-0650)^[22] and Christensen (PDF 01-082-0733).^[23] Additionally, the formation of Er_2SiO_5 was identified (green squares, PDF 01-077-6174).^[24] Notably, the intense peak at $2\theta \approx 70^{\circ}$, along with those at $2\theta \approx 14^{\circ}$ and 29° , originates from the silicon substrate. For the Yb-doped sample, the XRD spectrum (Figure 4b) confirms the exclusive formation of $\text{Yb}_2\text{Si}_2\text{O}_7$ (PDF 01-072-4438).^[25,26] These ternary phases align with the EDS and RBS results. Further RBS analysis (Figure 3) revealed minor Er and Yb peaks, suggesting limited deposition within the porous structure. However, the higher Er signal in the PS:Er (0.02M) sample correlates with the elevated $\text{Er}(\text{NO}_3)_3$ concentration in the precursor solution.

Although the electrochemical formation of RE silicates is uncommon in planar silicon, our results demonstrate their feasibility in PS. The formation of RE silicates requires SiO_2 as an oxygen and silicon source. In our samples, the presence of SiO_2 during RE doping can be attributed to two primary sources: the first one is linked to the native oxide, determined by the high reactivity of the porous surface—particularly in microporous structures, as observed in our samples. The second source is related to the ethanol-mediated SiO_2 formation during electrochemical etching in HF-based solutions. Ethanol influences the wetting behavior, surface chemistry, and oxidation kinetics,

thereby modulating porous structure development and subsequent SiO_2 formation. The rate of SiO_2 formation is ethanol-concentration-dependent: higher concentrations increase capillary stress during drying, enhancing SiO_2 formation, whereas lower concentrations slow this process.^[27] However, RE-silicate formation also depends on the presence of oxidizing species. The mixture of ethanol with $\text{Er}(\text{NO}_3)_3$ or $\text{Yb}(\text{NO}_3)_3$ used for doping fulfills this requirement, as NO_3^- acts as an active oxidizing agent in acidic media.^[28] The NO_3^- concentration directly influences SiO_2 formation, leading to increased RE-silicate formation, as evidenced by the enhanced absorbance spectra (Figure 5). During electrochemical infiltration, RE elements (Er or Yb) accumulate at pore walls, reacting with SiO_x to form $\text{RE}_2\text{Si}_2\text{O}_7$ or RE_2SiO_5 .

The observed increase in absorbance following thermal treatment can be attributed to an increase in the $\text{RE}_2\text{Si}_2\text{O}_7$ or RE_2SiO_5 formation, which is facilitated by the annealing procedure. However, the enhanced quantity of RE silicates also suggests the presence of RE_2O_3 oxides within the porous structure, despite their absence in XRD measurements, since the proposed reaction obeys Equation (2) and (3). While the optimal temperature for the formation of Er-silicates is $\approx 700\text{--}1100\text{ }^{\circ}\text{C}$,^[29,30] Yb-silicates typically require higher temperatures, ranging between 900 and $1200\text{ }^{\circ}\text{C}$.^[31] Nevertheless, in our study, even though the samples were annealed only at $900\text{ }^{\circ}\text{C}$, the highly reactive chemical surface of PS enables the formation of Yb-silicates at temperatures below $900\text{ }^{\circ}\text{C}$, although the presence of Yb_2SiO_5 was not detected.

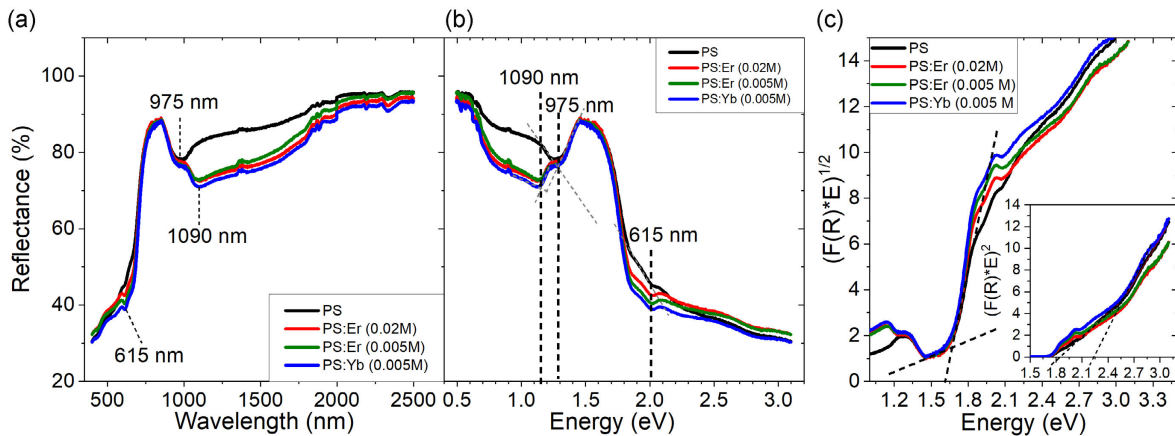
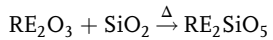
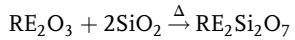


Figure 5. Reflectance spectrum from pristine, Er-deposited, and Yb-deposited samples as a function of the a) wavelength and b) photon energy. c) Tauc's plot from Kubelka-Munk data for indirect transition and direct transition (inset).



2.3. Optical Characterization

Figure 5a,b shows the reflectance spectra from PS:Er samples along with those measured from pristine PS. From these curves, the effect of Er into PS is to enhance the optical absorbance of the PS structures insofar as the amount of Er, which is more marked in the region of 1000 to 2000 nm (0.6 to 1.3 eV). Comparable results in absorbance improvement were reported using cerium and lanthanum.^[10–12] Since all samples were deposited the same number of cycles, the larger absorption of PS:Er(0.02M) is associated with the greater amount of Er deposited if compared with PS:Er (0.005M). The marked absorption observed in PS:Yb (0.005M) seems to be linked to the larger number of electrons of Yb than Er. From these curves, the PS energy bandgap, E_g , was estimated using the Kubelka-Munk method, following the procedure detailed in refs. [32,33]. Although PS has luminescence properties, prior work finds that it still preserves the indirect transition band of its planar counterpart, although some research groups consider a transition from indirect to direct transition associated with the quantum confinement effect.^[34,35] For this reason, the energy gap, E_g , of our samples was estimated by extrapolating the Kubelka-Munk curves, as is shown in Figure 5c through the dashed lines,^[32,33] and the results for the case of direct and indirect transition are summarized in Table 1, where E_{g1} refers to the optical E_g extracted by the linear extrapolation, following the Tauc plot method.

Although this method is typically employed for this aim, Makula et al.^[36] and Kelin et al.^[33] claim that adequate measurements of E_g should take into account some additional effects, such as the presence of two or more phases within the structure, as well as absorption tail, quantization effects, and so on. Since our sample is a porous matrix where the formation of ternary compounds based on Er (or Yb), Si, and O is shown by the EDS, RBS, and XRD analysis, it is reasonable to think that for

Table 1. Energy gap estimated from reflectance measurements using the Kubelka-Munk method.

| Samples | Indirect transition | | Direct transition | |
|--------------------|---------------------|---------------|-------------------|---------------|
| | E_{g1} [eV] | E_{g2} [eV] | E_{g1} [eV] | E_{g2} [eV] |
| PS pristine | 1.623 ± 0.025 | 1.67 ± 0.56 | 2.180 ± 0.022 | 2.58 ± 0.68 |
| PS:Yb (0.005 M Yb) | 1.648 ± 0.014 | 1.69 ± 0.69 | 2.215 ± 0.036 | 2.57 ± 0.74 |
| PS:Er (0.005 M Er) | 1.596 ± 0.021 | 1.63 ± 0.61 | 2.159 ± 0.028 | 2.55 ± 0.53 |
| PS:Er (0.02 M Er) | 1.642 ± 0.021 | 1.68 ± 0.71 | 2.246 ± 0.036 | 2.61 ± 0.62 |

measuring E_g , it is necessary to follow the procedure proposed by Makula et al.^[36] In Table 1, it was labeled as E_{g2} . These results show that E_g measured is larger than that for silicon ($E_g = 1.124$ eV at room temperature, computed from Si absorbance curve in Figure 6) and is coherent for a porosity of ≈55%, as reported in the literature.^[35] The nonsignificant changes in E_g , even after Er (or Yb) incorporation, indicate samples with comparable porosities and thicknesses, as expected, because all samples were obtained using the same electrochemical parameters and the same substrate. This suggests that the incorporation of Er or Yb into the porous matrix does not affect E_g . However, the increasing peaks at 615 (2.01 eV) and 1090 nm (1.13 eV) indicate the possible presence of the ternary compounds $\text{RE}_2\text{Si}_2\text{O}_7$ (RE = Er, Yb) in the absorption process. This observation aligns with the findings of Filippov et al.^[37] and other authors,^[38,39] where they highlighted the correlation between these peaks and the absorption/emission wavelengths of Er and Yb, suggesting that the heightened absorption in the 1000–2000 nm range is due to light absorption by Er^{3+} or Yb^{3+} from these ternary compounds. However, the participation of the surface roughness is also possible.

Figure 6a depicts the absorbance measurements of Er- and Yb-incorporated PS along the whole wavelength range, both before and after thermal oxidation, compared to as-etched PS and a planar silicon substrate for reference. It is evident that the absorbance of the as-etched PS is higher than that of the silicon substrate, showing maxima around 400 nm. This value decreases

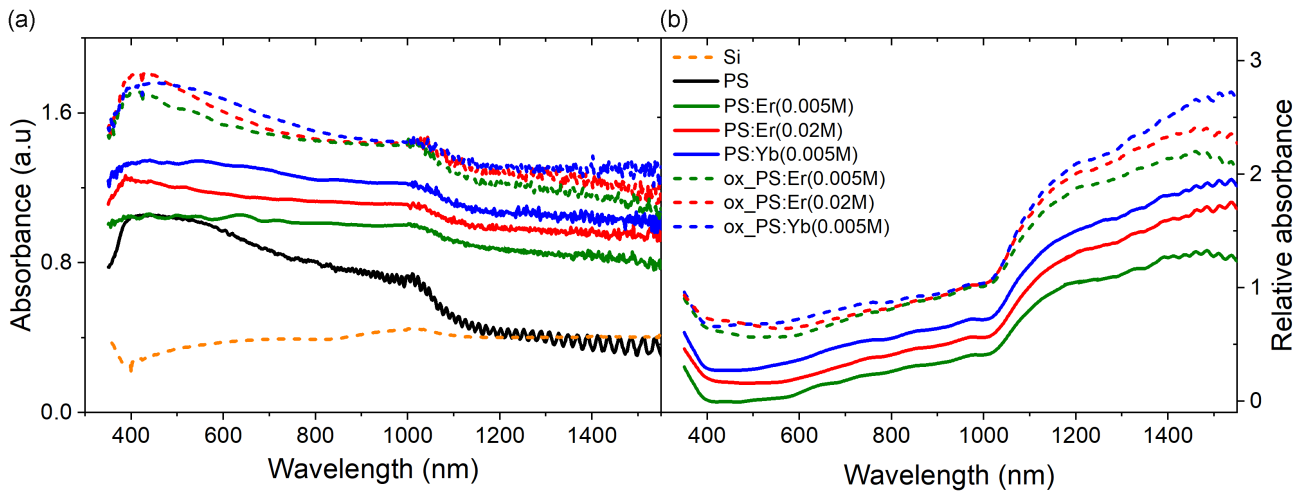


Figure 6. a) Absorbance spectra of as-deposited PS (solid lines) and after thermal oxidation at 300 °C (5 min) followed by an additional annealing step at 900 °C (5 min) (dashed lines), measured at varying Er and Yb concentrations. Spectra for as-etched PS (black solid line) and the silicon substrate (orange solid line) are included for reference. b) Corresponding relative absorbance profile.

progressively, exhibiting interference fringes typical of thin films. The reduction in absorbance is linked to a decreasing extinction coefficient, the reason why silicon becomes transparent in the infrared region, as reported by different research groups^[40,41] and supported by the effective medium theory.^[42] Figure 6b exhibits the average absorbance relative to the as-etched PS. It is seen in this figure that doping with 0.005M $\text{Er}(\text{NO}_3)_3 \cdot 5\text{H}_2\text{O}$ leads to an enhancement in absorbance by $\approx 100\%$ at 1200 nm and 120% at 1550 nm. This improvement is even more pronounced in PS:Er(0.02), where the absorbance reaches $\approx 130\%$ and 170% at these wavelengths. On the other hand, while the Yb concentration in PS:Yb(0.005) is comparable to that of Er in PS:Er(0.005), its absorbance surpasses 170% at wavelengths above 1200 nm. This behavior is consistent with previous studies involving RE elements such as cerium, lanthanum, and samarium,^[10,14] where the enhanced absorption was attributed to increased surface roughness and silicon particle growth. Atayaoui et al.^[10–12] attribute the observed increase in absorbance to the formation of a new layer during the doping process, as well as light absorption by deposited metal phases. However, this explanation does not align with our findings, as XRD analysis (Figure 4) confirms the absence of any metallic phase in our samples. Instead, Zarraoug et al.^[14] propose that the primary mechanism for enhanced absorbance in as-etched porous silicon (PS) is light scattering and trapping within its porous structure. They further suggest that after sintering, the rise in light absorption is linked to a phase transformation from silicon to silicates. The influence of these defects and phase transitions on the optical properties of silicon-based materials was recently reviewed by Cao et al.^[43] Their findings suggest that such defects enhance light scattering, thereby improving light absorption.

Notably, after thermal oxidation, the absorbance values rise significantly, reaching between 200% and 300% at 1550 nm (see dashed line curves in Figure 6). This increase is likely due to the formation of rare-earth-based ternary compounds, as indicated by EDS (Figure 2c,d) and XRD (Figure 4) analyses,

since in untreated PS oxidation reduces surface roughness^[40] and the presence of SiO_2 in the porous structure generally decreases optical absorption in the visible spectrum,^[44,45] reason by which the overall absorbance in the infrared region vanishes.

As previously mentioned, the thickness and porosity of all samples were estimated from these spectra using a single-layer model on a substrate in conjunction with the Looyenga model.^[15,16] Strümpel et al.^[46] have suggested that for solar cell applications, it is crucial to enhance absorption at wavelengths above 1100 nm, corresponding to energies below the silicon bandgap ($E < 1.12 \text{ eV}$). Figure 6 demonstrates that this condition is met, particularly after the incorporation of Er or Yb, with further improvement observed following thermal oxidation. Thus, the incorporation of Er or Yb into the PS matrix holds great potential for photovoltaic applications, similar to findings with cerium, lanthanum, and samarium.^[10,14] However, further experimentation is needed to fully validate the effects of Er and Yb in this context. This constitutes our next research objective.

2.4. Electrochemical Impedance Spectroscopy Analysis

Figure 7a–c presents typical Nyquist plots obtained from electrochemical impedance spectroscopy (EIS) measurements under open-circuit potential (OCP) conditions, both before and after Er or Yb deposition via the cyclic voltammetry method. Corresponding Bode plots are shown in Figure 7d–f. These characterizations were conducted immediately following the production of PS, which was then rinsed with distilled water and ethanol to remove residual water from the pores and expedite the drying process. A reduction in resistance upon rare earth deposition was observed in all samples.

When comparing different electrolyte concentrations, the higher concentration (0.02 M, Figure 6a) exhibited lower resistance, consistent with the increased presence of RE ions in the ethanolic solution and the greater amount of Er or Yb into

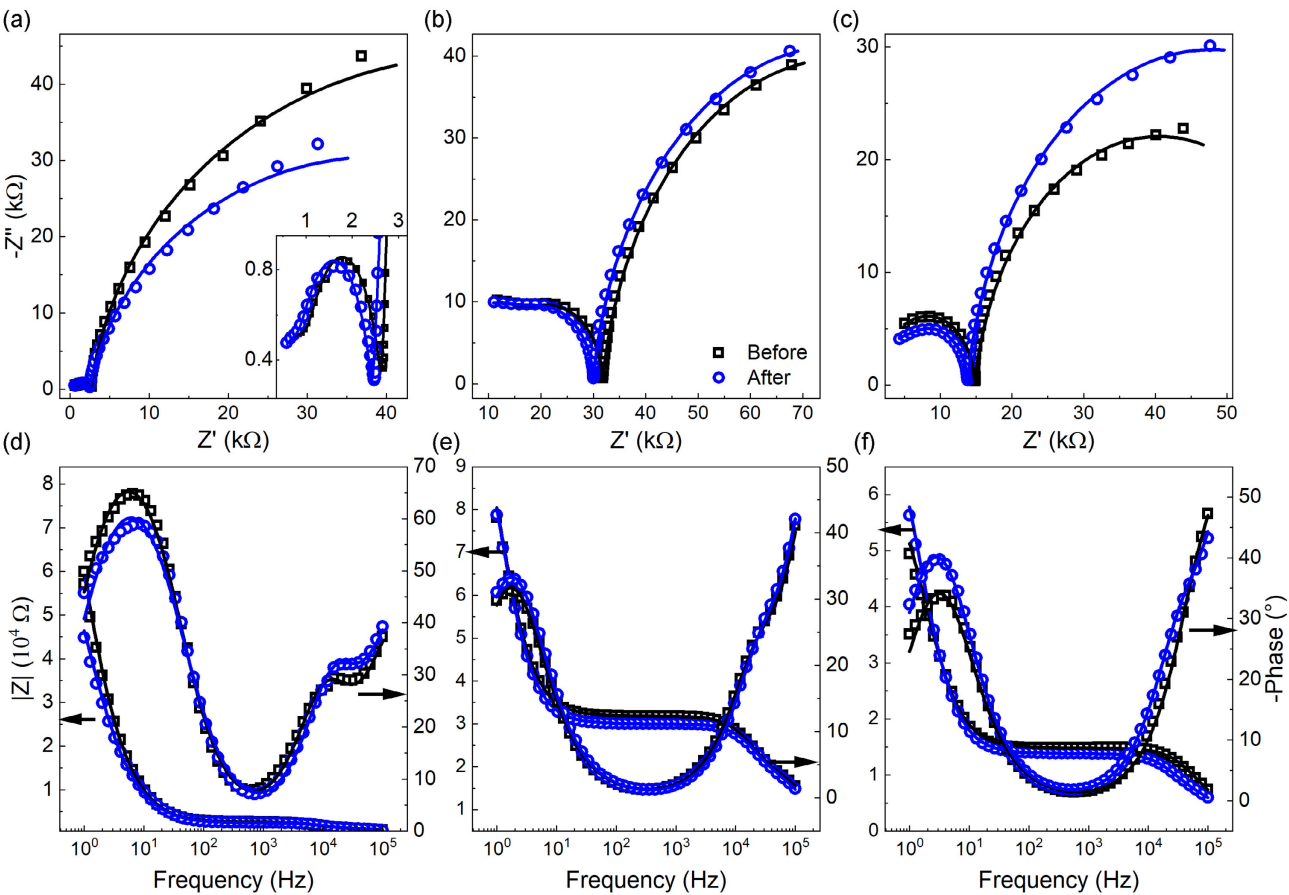


Figure 7. Nyquist plots extracted from EIS spectra measured of PS respectively in a) 0.02 M and b) 0.005 M $\text{Er}(\text{NO}_3)_3 \cdot 5\text{H}_2\text{O}$ electrolyte; along with c) 0.005 M $\text{Yb}(\text{NO}_3)_3 \cdot 5\text{H}_2\text{O}$ ethanolic, while its corresponding modulus and phase Bode plots are placed in (d–f). Experimental data were plotted in unfilled black square symbols (as-etched), and unfilled blue circles are designed for the as-RE deposited PS matrixes. The black and blue solid curves are the fitting curves.

the porous structure. This is evidenced by the reduced semicircular feature in the high-frequency region of the Nyquist plots. However, at low frequencies, an apparent increase in resistance is observed in samples PS:Er(0.02 M) and PS:Er(0.005 M) since the semicircle feature radii increase. The increase in resistance is also evident in the modulus of the Bode plot (Figure 7d–f). Typically, an increase in the low-frequency regions is associated with a rise in charge transfer resistance (R_{ct}) across the double electrical layer between the electrolyte solution and the PS surface. This is due to the reciprocal relationship between R_{ct} and the exchange current.^[17,18] For silicon-based electrodes, this resistance increase may be attributed to partial oxidation of the PS surface, even in ethanolic solutions.^[20] However, a definitive interpretation can only be made after fitting the EIS data. Furthermore, three distinct relaxation processes are discernible: two overlapping in the high-frequency region and one in the low-frequency region, as confirmed by the Bode plots. These relaxation processes likely correspond to different mechanisms of charge accumulation.

To quantify the EIS data, the electrical equivalent circuit (EEC) depicted in Figure 8 was proposed. This circuit incorporates constant phase elements (CPEs) to account for the capacitive

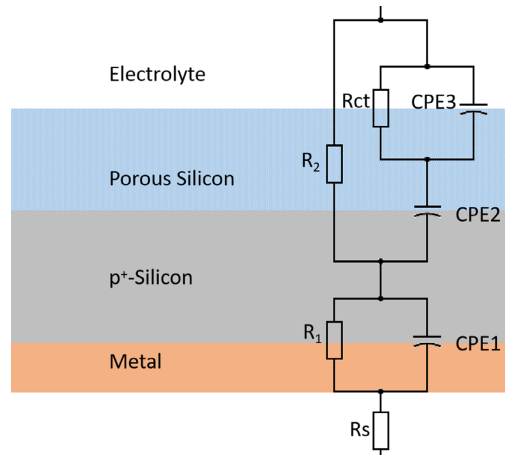


Figure 8. EEC schematic representation used in EIS analysis.

behavior at the electrolyte/PS, PS/bulk silicon, and bulk silicon/metal interfaces. The use of CPEs is intended to regard the nonhomogeneities on the PS surface, which are associated with interface roughness and, consequently, a heterogeneous

time distribution. This EEC approach has been effective in modeling similar devices.^[47] As shown in Figure 8, the PS phase is treated as an effective layer, with all interfaces connected in series. Additionally, each CPE is connected in parallel with a resistor, representing the charge transfer resistance. Due to the PS porosity, the charge transfer resistance (R_2) is in parallel with both CPE2 and CPE3, as the electrolyte can penetrate the effective PS layer. CPE3 corresponds to the Helmholtz double layer. For this model, the frequency-dependent impedance associated with each CPE is written as a function of the ideality coefficient n as^[48]

$$Z_{\text{CPE}} = \frac{1}{Q} (j\omega)^{-n} \quad (4)$$

The results of the EEC modeling are presented in **Table 2**. Figure 7 shows the fitting curves, depicted as solid lines, demonstrating good agreement with the experimental data, albeit with some dispersion at low frequencies. It is observed that the incorporation of Er (or Yb) significantly alters the electrical properties of the samples, as anticipated. The Nyquist plots in Figure 7a–c suggest that the observed changes correlate with a reduction in PS resistivity, likely due to RE ion incorporation, which enhances charge transfer. However, EIS fitting procedure reveals a more intricate charge transfer mechanism. Given the inherent heterogeneity and stochastic nature of PS porosity formation, not all resistance values follow the same trend, as porosity is strongly influenced by the experimental conditions' kinetics and thermodynamics. Nevertheless, the resistances remain consistent in order of magnitude, indicating a robust fit despite the morphological complexity introduced by porosity. Notably, R_2 exhibits the highest resistance values, which are primarily associated with the contribution of the electrolyte because of the poor electrical conduction of the ethanol through the porous structure. The incorporation of RE ions into the solution typically enhances conductivity; consequently, the observed increase in R_2 is attributed to the formation of RE silicates within the doped porous matrix, as corroborated by XRD analysis (Figure 4). While a modest 1.5% rise in R_2 occurs with 0.005 M Er doping, this effect intensifies significantly ($\approx 22\%$) at the same concentration of Yb. Notably, a higher Er concentration (0.02 M) reduces R_2 by

Table 2. Parameters extracted by fitting the EIS data before and after RE deposition.

| Parameters | 0.02 M $\text{Er}(\text{NO}_3)_3$ | | 0.005 M $\text{Er}(\text{NO}_3)_3$ | | 0.005 M $\text{Yb}(\text{NO}_3)_3$ | |
|-----------------------------|-----------------------------------|--------|------------------------------------|---------|------------------------------------|--------|
| | Before | After | Before | After | Before | After |
| $R_s (\Omega)$ | 268.91 | 205.96 | 714.09 | 700.81 | 1112 | 645.99 |
| $R_1 (\Omega)$ | 1606.6 | 1544 | 15 953 | 15 261 | 2351.9 | 4826.6 |
| $R_2 (\Omega)$ | 99 477 | 74 184 | 106 150 | 107 730 | 62 727 | 76 443 |
| $R_{ct} (\Omega)$ | 748.12 | 663.62 | 17 607 | 16 079 | 13 822 | 9320 |
| $Q_1 (\text{pF cm}^{-2})$ | 170.0 | 119.0 | 0.733 | 0.785 | 4.97 | 2.54 |
| n_1 | 0.984 | 0.995 | 0.997 | 1.0 | 0.993 | 0.996 |
| $Q_2 (\text{nF cm}^{-2})$ | 2.09 | 2.28 | 0.725 | 0.606 | 0.428 | 0.896 |
| n_2 | 1.0 | 0.996 | 0.989 | 1.0 | 0.971 | 0.991 |
| $Q_3 (\mu\text{F cm}^{-2})$ | 2.35 | 3.01 | 1.80 | 1.80 | 1.87 | 2.05 |
| n_3 | 0.922 | 0.882 | 0.913 | 0.919 | 0.903 | 0.914 |

25.4%, highlighting the competing influences of ionic conductivity and RE silicate formation. Despite these variations in RE type and concentration, interfacial charge transfer consistently improves. This is evidenced by an $\approx 11\%$ reduction in R_{ct} for the 0.02 M Er-doped sample compared to its undoped counterpart. However, the enhancement is substantially greater with 0.005 M Yb doping, yielding a $\approx 33\%$ decrease in R_{ct} .

On the other hand, R_1 and R_2 represent charge transfer at the metal/semiconductor and Si/PS interfaces, respectively. The magnitude of these parameters indicates rectifying behavior, attributable to space charges in both semiconductors. This is further corroborated by the parametric values of the constant phase elements. CPE1 and CPE2 exhibit n close to one, suggesting interfacial behavior similar to that of a capacitor with minimal time constant dispersion. This can be attributed to the bulk monocrystalline p⁺-Si, which possesses a nearly homogeneous structure. The EEC analysis yields a capacitance on the order of nF cm^{-2} , indicative of space charge capacitance at high frequencies. Consequently, the two convoluted relaxation processes observed at high frequency in Figure 7 are identified as space charge responses from the PS and bulk Si semiconductors, both having similar time constants. CPE3 likely corresponds to the electrolyte/PS interface, characterized by a double-layer capacitance. This interpretation is supported by the appearance of a semicircular arc at low frequencies in the Nyquist plot and a corresponding phase peak in the Bode plot (Figure 7). The capacitance values are on the order of $\mu\text{F cm}^{-2}$, consistent with double-layer capacitance. Additionally, n for these samples ranges from 0.88 to 0.92, lower than those associated with space charge (which approach one). This reduction is due to the heterogeneity of the PS surface porosity, which leads to a distribution of time constants.

3. Conclusions

Erbium and ytterbium were deposited into mesoporous silicon using the cyclic voltammetry method. The results indicate that this method is optimal for rare earth deposition due to its non-reversible nature in silicon, which favors the incorporation of RE into the porous silicon structure while inhibiting its removal. Chemical analyses using EDS, RBS, and XRD confirm the successful incorporation of both erbium and ytterbium into PS. Furthermore, in Er-doped PS, XRD analysis reveals the formation of ternary compounds Er_2SiO_5 and $\text{Er}_2\text{Si}_2\text{O}_7$. In contrast, only the formation of $\text{Yb}_2\text{Si}_2\text{O}_7$ is observed for ytterbium under the same electrochemical conditions. Optical analyses using reflectance and absorbance measurements indicate that the presence of erbium or ytterbium enhances the absorbance of PS. This absorbance increases with higher concentrations of erbium, but when erbium is substituted by ytterbium, the absorbance becomes even greater than in PS doped with erbium alone. The increase in absorbance, even in the visible region, suggests that RE incorporation could be an effective method to enhance the absorbance of photovoltaic cells. Here, this device was not characterized. The EIS analysis further reveals that incorporating RE elements improves charge transfer between the porous substrate and the liquid medium. This enhancement depends on both the RE doping concentration and the specific RE element

used. At a fixed doping level, Yb reduces the charge transfer resistance nearly threefold compared to Er. However, the substrate conductivity exhibits greater sensitivity to the RE concentration. When doped with 0.02 M Er, the porous matrix resistance decreases by $\approx 25.4\%$, whereas a lower concentration (0.005 M Er) results in a slight increase (1.5%) in resistance. This behavior suggests a delicate interplay between charge transport within the RE silicates in the porous structure and interfacial charge transfer.

4. Experimental Section

Sample Preparation: The fabrication of the samples involved a three-step process. Initially, p^+ -type substrates, with a resistivity of $0.2 \Omega \cdot \text{cm}$, were cleaned by immersion in a solution of $\text{H}_2\text{SO}_4:\text{H}_2\text{O}:\text{H}_2\text{O}_2$ (2:1:1) at 90°C for 30 min, followed by rinsing in distilled water for 5 min, for organic impurity removal. Subsequently, the substrates were treated in a solution of $\text{HNO}_3:\text{H}_2\text{O}:\text{H}_2\text{O}_2$ (1:5:1) at 70°C for 10 min, for organic impurities subtraction. The samples were anodized in an electrochemical cell with an HF:ethanol solution (3:1) v/v. The current density was set at 20 mA cm^{-2} for 20 min. Finally, ionic Er and Yb were deposited using the cyclic voltammetry method using PS as the working electrode and platinum grade as a counter electrode, along with an electrode reference of Ag/AgCl. For this aim, ethanoic solutions of 0.005 and 0.02 M $\text{Er}(\text{NO}_3)_3 \cdot 5\text{H}_2\text{O}$ and 0.005 M $\text{Yb}(\text{NO}_3)_3 \cdot 5\text{H}_2\text{O}$ were employed as electrolytes. These reagents, with purity of 99.9%, were purchased from Sigma-Aldrich. The deposition procedure was made immediately after PS formation, by substituting the HF-based electrolyte used for pore formation with the RE-based ethanolic solution. Prior to this substitution, the electrochemical cell containing the as-etched PS was cleaned with deionized water to eliminate HF. For the RE deposition, the experimental parameters were adjusted for potential scan between -1.5 and 0.6 V at 100 mV s^{-1} of sweep for ten cycles. This procedure was carried out using a PGSTAT302N AUTOLAB potentiostat, with the electrochemical parameters being set through the NOVA 2.1 software.

After Er or Yb deposition, the samples were optically passivated by two-step thermal oxidation: 5 min at 300°C and then an additional 5 min at 900°C in an air environment. The thermal oxidation step was essential to create a stable oxide layer on the surface of the samples, providing protection and passivation. This enabled further characterization and analysis of the as-deposited RE (Er or Yb) layers.

Characterization: Morphological analysis was conducted using a scanning electron microscope, specifically, a Carls Zeiss Model EVO MA15, equipped with a TLD-SE detector. This instrument also facilitated chemical characterization via energy-dispersive X-ray spectroscopy (EDS), with a focus on $\approx 1 \mu\text{m}$ of the electron beam across the entire PS:Er or PS:Yb surface. Additional chemical characterization was carried out by XRD using an X-pert Panalytical, and Rutherford Backscattering (RBS) by incoming 4He^+ ions accelerated to 2.2 MeV on the sample surface. For data recording, the sensor was placed at 170° . These techniques allowed for a comprehensive analysis of the morphological and chemical properties of the PS:Er (or PS:Yb) surface, providing valuable insights into its structure and composition for the research study.

The optical properties were characterized by recording the reflectance with the aid of a Shimadzu photospectrometer equipped with an integrating sphere. The absorbance was measured by a spectrometer equipped with an optical fiber. For both experiments, a commercial aluminum mirror was used as a reference.

For EIS characterization, the working electrodes were as-etched and as-rare-earth deposited PS, using FRA32M module of the same AUTOLAB potentiostat employed for RE deposition. Initially, the OCP was determined, followed by the application of a sinusoidal alternating current signal with an amplitude of 10 mV. To avoid artifacts due to equipment limitations at high frequencies and faradaic reactions at low frequencies, the FRA (frequency response analyzer) response was measured in 1 Hz to

100 kHz range, using the ethanolic solution used for rare earth deposition as electrolyte EIS measurements were performed at the OCP condition both before and after RE deposition.

Acknowledgements

The author gratefully acknowledges the Laboratório de Caracterização Estrutural (LCE) from Federal University of Itajubá for providing access to the SEM and XRD equipment. This research was financially supported by the Fundação de Amparo à Pesquisa do Estado de Minas Gerais (FAPEMIG) under grant APQ-01419-24.

The Article Processing Charge for the publication of this research was funded by the Coordenação de Aperfeiçoamento de Pessoal de Nível Superior - Brasil (CAPES) (ROR identifier: 00x0ma614).

Conflict of Interest

The authors declare no conflict of interest.

Data Availability Statement

The data that support the findings of this study are available from the corresponding author upon reasonable request.

Keywords

absorption enhancement, deposition of rare earths, porous silicon

Received: May 19, 2025

Revised: September 3, 2025

Published online: September 22, 2025

- [1] A. Loni, *Handbook of Porous Silicon*, 2nd ed. (Ed: L. Canham), Springer, Switzerland **2018**, pp. 13–24.
- [2] M. J. Sailor, E. C. Wu, *Adv. Funct. Mater.* **2009**, *19*, 3195.
- [3] T. Chvojka, V. Vrkoslav, I. Jelínek, J. Jindrich, M. Lorenc, J. Dian, *Sens. Actuators B Chem.* **2004**, *100*, 246.
- [4] S. A. Sokolov, R. Rösslhuber, D. M. Zhigunov, N. V. Latuhina, V. Y. Timonhenko, *Thin Solid Films* **2014**, *562*, 462.
- [5] H. Elhouichet, M. Oueslati, *Phys. Status Solidi A* **2007**, *204*, 1497.
- [6] B. González-Díaz, B. Díaz-Herrera, R. Guerrero-Lemus, J. Méndez-Ramos, V. D. Rodríguez, C. Hernández-Rodríguez, J. M. Martínez-Duart, *Mater. Sci. Eng. B* **2008**, *146*, 171.
- [7] G. Mula, E. Pinna, A. Falqui, R. Ruffilli, S. Palmas, M. Mascia, *Appl. Surf. Sci.* **2014**, *311*, 252.
- [8] V. Petrovich, S. Volchek, L. Dolgyi, N. Kazuchits, V. Yakovtseva, V. Bondarenko, *J. Porous Mater.* **2000**, *7*, 37.
- [9] T. Trupke, A. Shalav, B. S. Richards, P. Würfel, M. A. Green, *Sol. Energy Mater. Sol. Cells* **2006**, *90*, 3327.
- [10] M. Atyaoui, W. Dimassi, A. Atyaoui, J. Elyagoubi, R. Ouertani, H. Ezzaouia, *J. Lumin.* **2013**, *141*, 1.
- [11] M. Atyaoui, W. Dimassi, M. Khalifa, R. Chtourou, H. Ezzaouia, *J. Lumin.* **2012**, *132*, 2572.
- [12] M. Atyaoui, M. Dimassi, G. Monther, R. Chtourou, H. Ezzaouia, *J. Lumin.* **2012**, *132*, 277.
- [13] R. F. Muniz, V. S. Zanuto, M. S. Gibin, J. V. Gunha, A. Novatski, J. H. Rohling, A. N. Medina, M. L. Baesso, *J. Rare Earths* **2023**, *41*, 342.
- [14] A. Zarroug, Z. Bouznif, Z. B. Hamed, L. Derbali, H. Ezzaouia, *Int. J. Adv. Manuf. Technol.* **2017**, *93*, 2403.

- [15] O. Stenzel, *The Physics of Thin Film Optical Spectra*, 2nd ed., Springer, Switzerland **2016**, pp. 131–161.
- [16] H. Looyenga, *Physica* **1965**, *31*, 401.
- [17] E. Gileadi, *Physical Electrochemistry – Fundamentals, Techniques and Applications*, Wiley-VHC, Weinheim **2011**, pp. 221–236.
- [18] C. M. A. Brett, A. M. O. Brett, *Electrochemistry – Principles, Methods, and Applications*, Oxford University Press, New York **1994**, pp. 174–198.
- [19] M. H. Joo, S. J. Park, S. M. Hong, C. K. Rhee, Y. Sohn, *Materials* **2020**, *13*, 5314.
- [20] X. G. Zhang, *Electrochemistry of Silicon and Its Oxide*, Kluwer Academic Publishers, New York **2004**, pp. 1–90.
- [21] P. Vanýsek, *Handbook of Chemistry and Physics*, 97th ed. (Ed: W. M. Haynes), Vol.8, CRC Press, Boca Raton **2016**, pp. 20–29.
- [22] Y. I. Smolin, Y. F. Shepelev, *Acta Cryst.* **1970**, *B26*, 484.
- [23] A. N. Christensen, *Z. Krist.–Cryst. Mater.* **1994**, *209*, 7.
- [24] D. Phanon, R. Cerny, Z. Anorg. Allg. Chem. **2008**, *634*, 1833.
- [25] A. J. Fernández-Carrión, M. D. Alba, A. Escudero, A. I. Becerro, *J. Solid State Chem.* **2011**, *184*, 1882.
- [26] A. Velden, M. Jansen, *Z. Anorg. Allg. Chem.* **2004**, *630*, 234.
- [27] M.-T. Tsai, Y.-C. Lee, Y.-M. Lin, V. K. S. Hsiao, C.-C. Chu, *Materials* **2024**, *17*, 989.
- [28] M. Steinert, J. Acker, K. Wetzig, *J. Phys. Chem. C* **2008**, *112*, 14139.
- [29] R. L. Savio, M. Miritello, F. Iacona, A. M. Piro, M. G. Grimaldi, F. Priolo, *J. Phys: Condens. Matter* **2008**, *20*, 454218.
- [30] J. Li, Z. Sun, *J. Lumin.* **2012**, *132*, 325.
- [31] N. Wu, Y. Wang, R. Liu, Q. Wen, H. Liu, X. Xiong, *Ceram. Int.* **2022**, *48*, 11545.
- [32] P. R. Jubu, E. Danladi, U. I. Ndeze, O. Adedokun, S. Landi Jr, A. J. Haider, A. T. Adepoju, Y. Yusof, O. S. Obaseki, K. F. Yam, *Results Opt.* **2024**, *14*, 100606.
- [33] J. Klein, L. Kampermann, B. Mockenhaupt, M. Behrens, J. Strunk, G. Bacher, *Adv. Funct. Mater.* **2023**, *33*, 2304523.
- [34] J. T. Frederiksen, P. G. Melcher, E. Veje, *Phys. Rev. B* **1998**, *58*, 8020.
- [35] A. Mortezaali, S. R. Sani, F. J. Jooni, *J. Non-oxide Glasses* **2009**, *1*, 293.
- [36] P. Makula, M. Pacia, W. Macyk, *J. Phys. Chem. Lett.* **2018**, *23*, 6814.
- [37] V. V. Filippov, V. V. Kuznetsova, V. S. Homenko, P. P. Pershukevich, V. A. Yakovtseva, M. Balucani, B. P. Bondarenko, G. Lamedica, F. Ferrari, *J. Lumin.* **1999**, *80*, 395.
- [38] A. M. Smirnov, A. P. Bazakutsa, Y. K. Chamorovskiy, I. A. Nechepurenko, A. V. Dorofeenko, O. V. Butov, *ACS Photonics* **2018**, *5*, 5038.
- [39] S. Unger, A. Schwuchow, J. Dellith, J. Kirchhof, *Opt. Mater. Express* **2020**, *10*, 907.
- [40] K. Kordás, A. E. Pap, S. Beke, S. Leppävuori, *Opt. Mater.* **2004**, *25*, 251.
- [41] M. A. Green, *Sol. Energy Mater. Sol. Cells* **2008**, *92*, 1305.
- [42] D. R. Huanca, W. J. Salcedo, *Phys. Status Solidi A* **2015**, *212*, 1975.
- [43] H. Cao, X. Peng, F. Shi, Y. Tian, L. Kong, M. Chen, Q. Hao, *J. Mater. Res. Technol.* **2025**, *35*, 809.
- [44] J. Charrier, V. Alaiwan, P. Pirasteh, A. Najar, M. Gadonna, *Appl. Surf. Sci.* **2007**, *253*, 8632.
- [45] A. V. Pavlikov, A. V. Lartsev, I. A. Gayduchenko, V. Y. Timoshenko, *Microelectron. Eng.* **2012**, *90*, 96.
- [46] S. Strümpel, M. McCann, G. Beaucarne, V. Arkhipov, A. Slaoui, V. Srvcuk, C. del Cañizo, I. Tobias, *Sol. Energy Mater. Sol. Cell* **2007**, *91*, 238.
- [47] G. Mula, M. V. Tiddia, R. Ruffilli, A. Falqui, S. Palmas, M. Mascia, *Thin Solid Films* **2014**, *556*, 311.
- [48] H. Cesiulis, N. Tsyntsaru, A. Ramanavicius, G. Ragoisha, *Nanostrutures and Thin Films For Multifunctional Applications* (Eds: I. Tiginianu, P. Topala, V. Ursaki), Springer, Switzerland **2016**, pp. 3–42.